





Interaction and co-assembly of optical and topological solitons

Guilhem Poy^{1,2}, Andrew J. Hess³, Andrew J. Seracuse³, Michael Paul³, Slobodan Žumer^{1,4} and Ivan I. Smalyukh^{1,3,5,6}  

Solitons attract a great deal of interest in many fields, ranging from optics to fluid mechanics, cosmology, particle physics and condensed matter. However, solitons of these very different types rarely coexist and interact with each other. Here we develop a system that hosts optical solitons coexisting with topological solitonic structures localized in the molecular alignment field of a soft birefringent medium. We experimentally demonstrate and theoretically explain optomechanical interactions between such optical and topological solitons, mediated by the local transfer of momentum between light and matter and the nonlocal orientational elasticity of the liquid-crystal phase used in our system. We show that the delicate balance arising from these different contributions to the optomechanical force enables facile dynamical control and spatial localization of topological solitons. Our findings reveal unusual solitonic tractor beams and emergent light-matter self-patterning phenomena that could aid in creating new breeds of nonlinear photonic materials and devices.

Solitons are ubiquitous in nature and technology¹. They are found as water waves, pulses of light, wavefunctions of Cooper pairs in superconducting Josephson junctions, propagating pulses in biomembranes and nervous systems^{1–4}, models of elementary particles⁵ and even cosmological objects like black holes^{6–8}. An optical soliton generally refers to an optical waveform that maintains its shape when evolving over long distances and/or times, and even after collisions. This concept now encompasses a broad class of wavepackets with multiple spatial and temporal dimensions⁹. Having a particle-like nature, optical solitons can mutually attract, repel or yield fusion, fission and annihilation in media with nonlocal optical nonlinearities¹⁰.

Many recent studies have focused on optical solitons in liquid crystals (LCs). These soft birefringent media exhibit giant nonlinear and nonlocal optical responses, with a facile reorientation of their optical axis fields under external stimuli, enabling the generation of optical solitons at powers as low as ~ 1 mW. An archetypal example of optical solitons in LCs is the so-called nematicon, which propagates without diffracting by creating its own waveguide in the optical axis field of the LC^{11–13}. Trajectories of nematicons may be modified using optical reflections from dielectric interfaces and various deformed regions of the background optical axis field^{14–17}. Their potential for photonics applications has recently been demonstrated with mode transformations¹⁸, bistability^{19,20} and soliton-assisted random lasing²¹. Other types of optical solitons in LCs include discrete solitons²², optothermal and dark solitons in dye-doped LCs^{23,24}, self-focused beams with fast-evolving polarization states and spin-orbit interactions^{25–27}, and optical solitons in non-frustrated²⁸ or frustrated chiral LCs²⁹. At the same time, chiral LCs are also known to host a fascinating variety of topological solitons, like skyrmions, hopfions, torons and fingers^{30–34}, which correspond to localized and topologically protected patterns of the optical axis embedded within their uniform backgrounds \mathbf{n}_0 . These robust structures can be created on demand with strong external stimuli^{35,36}, they are stable

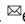
without external fields, and they cannot be continuously deformed into the uniform background \mathbf{n}_0 .

Discoveries of different types of laser light and matter interactions have had a strong impact on the development of fundamental science and technologies throughout recent history, from laser surgery to laser trapping of tiny particles, to laser cooling of atomic gases, and to the generation of Bose–Einstein condensates. However, to the best of our knowledge, none of these diverse forms of light–matter interactions have exploited the regime when both light and matter take solitonic embodiments.

Here, we experimentally discover and theoretically explain the fascinating interactions between topological solitons and two classes of optical solitons in LCs, thus showing how the particle-like nature of optical solitons enables optomechanical interactions with topological solitons. By focusing on a regime where each type of soliton is not perturbed too much, we experimentally characterize these interactions and theoretically explain them in an elegant and accurate manner with an effective Langevin equation that accounts for optical forces similar to the ones of optical traps, as well as nonlocal effects associated with the light-induced realignment of the optical axis field. The surprising findings within this new regime of light–matter interactions reveal that the interplay of nonlinear effects that stabilizes these different solitons can lead to the self-assembly of topological solitons beside the optical solitons. Such interactions yield exceptionally rich types of behaviour that may find practical uses ranging from nonlinear optics to nanophotonic devices and spatial light–matter co-patterning.

Results

Physics of inter-solitonic interactions and co-assembly. Our experimental investigations show that topological solitons in the optical axis of a uniaxial chiral nematic LC can not only be attracted or pushed away from the optical solitonic beam's axis but can also co-assemble in highly nontrivial ways (Fig. 1c) when forming

¹Faculty of Mathematics and Physics, University of Ljubljana, Ljubljana, Slovenia. ²Laboratoire Charles Coulomb, Univ Montpellier, CNRS, Montpellier, France. ³Department of Physics, University of Colorado, Boulder, CO, USA. ⁴Jožef Stefan Institute, Ljubljana, Slovenia. ⁵Chirality Research Center, Hiroshima University, Higashi Hiroshima, Japan. ⁶Renewable and Sustainable Energy Institute, National Renewable Energy Laboratory and University of Colorado, Boulder, CO, USA.  e-mail: ivan.smalyukh@colorado.edu

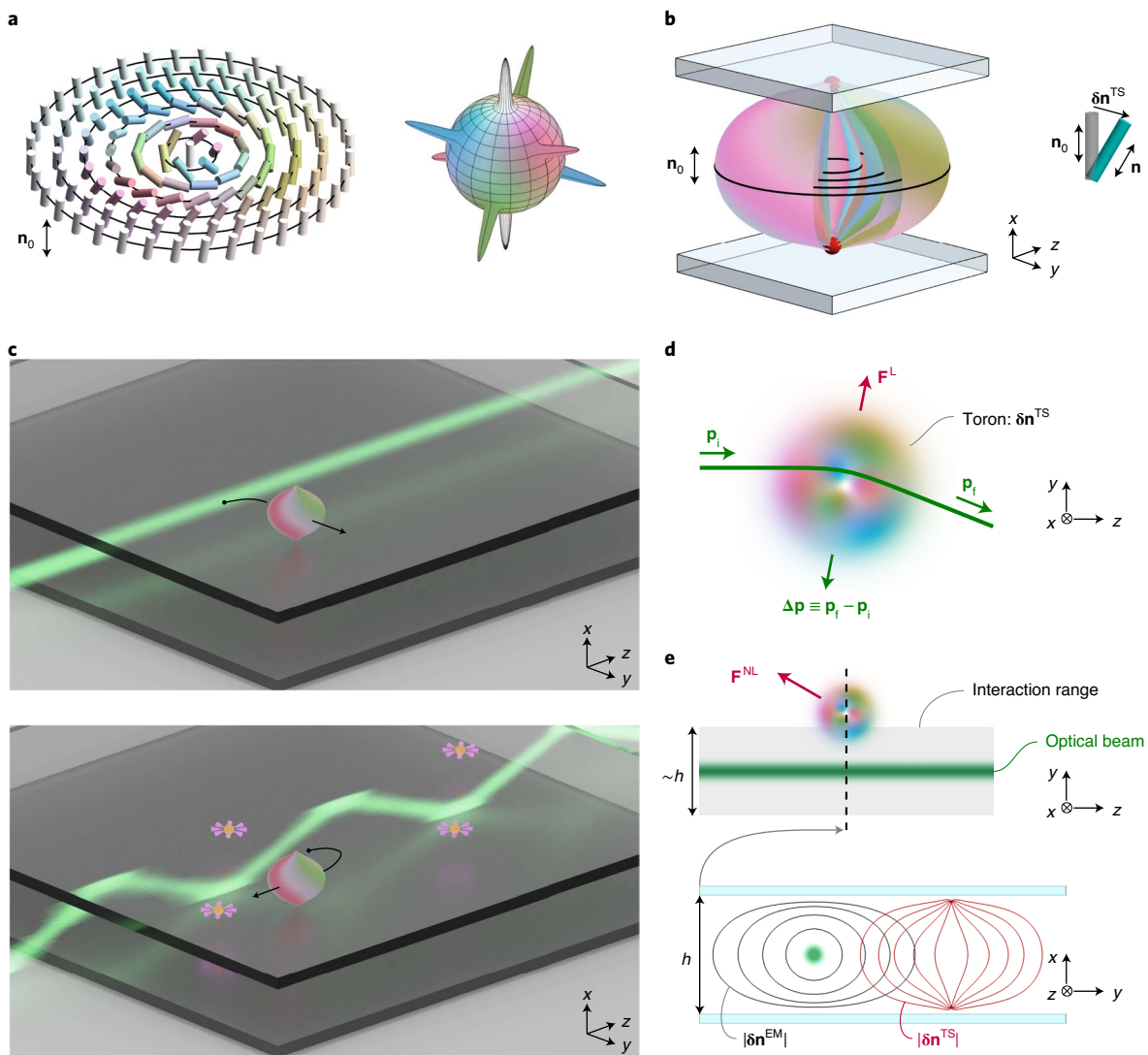


Fig. 1 | Host system with coexisting topological and optical solitons. **a**, Optical axis pattern of a baby skyrmion. Each nonpolar orientation of the optical axis is associated with a single colour. **b**, Toron embedding the optical axis pattern of **a** in the mid-sample plane. The confining plates impose the far-field optical axis orientation \mathbf{n}_0 . The inner black circles in **a** and **b** have a one-to-one correspondence and the red balls represent topological point singularities on which the baby skyrmion terminates while embedded in the uniform far-field background. The coloured surfaces are isosurfaces with fixed angles between \mathbf{n} and \mathbf{n}_0 . **c**, Schematic representation of the spin-orbit (top) and bouncing (bottom) optical solitons. The small spheres with pink converging arrows represent equilibrium points of the optical force field. **d**, The force \mathbf{F}^L arises from the conservation of momentum, when light rays are deflected by the toron's birefringent pattern. \mathbf{p}_i (\mathbf{p}_f) is the initial (final) momentum of light. **e**, The force \mathbf{F}^{NL} is related to the nonlocal elastic interactions between the optical axis patterns $\delta\mathbf{n}^{TS}$ (red isocontours) and $\delta\mathbf{n}^{EM}$ (black isocontours).

one-dimensional arrays of topological solitons localizing on the sides of the optical soliton. We experimentally reveal that this behaviour stems from the elaborate dynamical trajectories of topological solitons navigating their way when guided by particular optical solitons (Fig. 1c, bottom). What is the physical underpinning of this unexpected behaviour?

Our unwound chiral LC system is confined between glass plates, imposing an optical axis orientation \mathbf{n}_0 normal to the surfaces (see Methods). These samples host localized patterns of optical axis embedding an emblematic example of a topological soliton—the baby skyrmion—whose optical axis field is shown in Fig. 1a and whose name refers to Skyrme's topological solitons used to describe subatomic particles with different baryon numbers⁵. It covers twice the order parameter space of nonpolar unit vectors \mathbf{n} with antipodal symmetry $\mathbf{n} \leftrightarrow -\mathbf{n}$, that is, antipodal points on a sphere (Fig. 1a, right). To emphasize the topological and nonpolar

properties of these optical axis patterns, we introduce a colour scheme that associates an optical axis orientation with a colour. Our topological colouring is used for all cylindrical-glyph-based or continuous-colour plots of topological solitons and is detailed in Supplementary Section 2C, where we explain all the subtleties. For the skyrmion of Fig. 1a, one can easily check that white corresponds to the far-field optical axis \mathbf{n}_0 and that the primary colours blue, red and green (associated with tilted cylinders) appear twice. Each of these colours is associated with the antipodal peaks on the sphere of Fig. 1a. The two-dimensional structure of Fig. 1a corresponds to the mid-sample plane of the three-dimensional structure of Fig. 1b, which shows a few isosurfaces with fixed angles between \mathbf{n} and \mathbf{n}_0 . The quantity $\delta\mathbf{n}^{TS}$ corresponds to the deviation of the optical axis field \mathbf{n}^{TS} with respect to the far-field optical axis $\mathbf{n}_0 \equiv \mathbf{e}_z$ (unit vector of x-axis on Fig. 1) imposed by the confining plates and fully defines this class of topological structures called torons³², where 'TS' refers

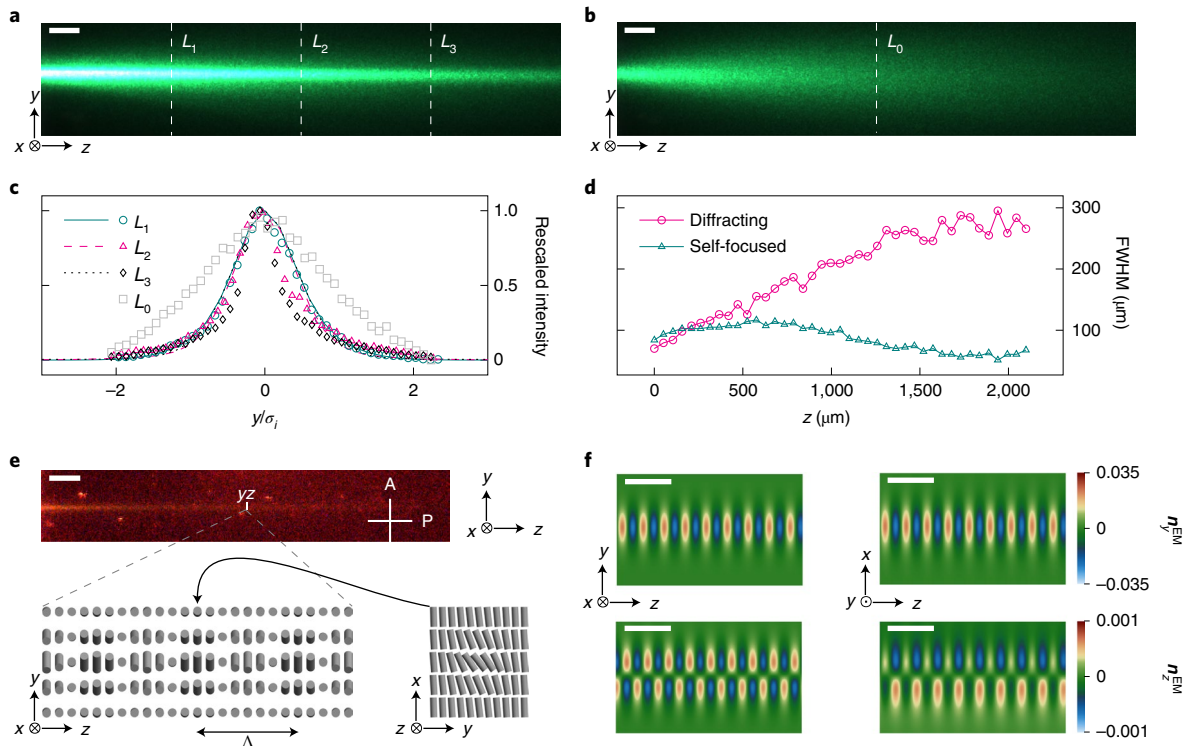


Fig. 2 | Properties of spin-orbit solitons. **a, b**, Optical micrographs of light scattered from a spin-orbit soliton with a beam power of 35 mW (**a**) and <1 mW (**b**). Scale bars, 100 μm . **c**, The transverse rescaled intensity profiles along the lines L_{0-3} in **a, b** as a function of y/σ_i , with σ_i the input FWHM. Symbols (lines) correspond to experimental (simulated) data. **d**, The FWHM values of the beams in **a, b** as a function of z . **e**, A polarised optical micrograph (POM) image of the optical soliton (top) and schematic representation of the associated simulated optical axis field of periodicity Λ in the yz and xy planes (bottom) with exaggerated reorientation angles and a stretched-out z direction. The orientations of polariser (P) and analyser (A) are indicated with a white cross. Scale bar, 100 μm . **f**, Cross-sections of the simulated optical axis pattern associated with a spin-orbit soliton in a 20- μm -thick sample. Since the optical axis field has a unit-norm and is only weakly deformed, we show only its y and z components. Scale bars, 5 μm .

to topological solitons. Although more complex torons³² and other solitons³⁰⁻³⁴ can be realized, our study in this work focuses solely on the simplest type of elementary toron depicted in Fig. 1. Further details are given in Supplementary Section 2A.

We consider the light-matter interactions of torons with two classes of optical soliton. The first class (Fig. 1c, top) corresponds to a beam propagating parallel to the confining plates of the sample, with a polarization state evolving in the xy plane orthogonal to the axis of propagation z . The second class (Fig. 1c, bottom) corresponds to a beam bouncing between the two confining plates due to total internal reflection, with a polarization state evolving in the xz plane aligned with the axis of propagation. Owing to the facile response of LCs to fields, both types of beam, when associated with an optical power that is sufficiently high (typically 1–100 mW), introduce a nonzero deviation $\delta\mathbf{n}^{\text{EM}}$ of the optical axis field \mathbf{n}^{EM} with respect to the far-field \mathbf{n}_0 , which enables their self-focusing. However, the physical origins of the self-focusing are different: in the first class, the self-focusing is due to the giant spin-orbit interactions arising from the Pancharatnam-Berry phase of uniaxial LCs^{25,26}, which define an effective waveguide for the mutually coupled and orthogonal photonics mode of propagation with extraordinary/ordinary polarization; in the second class, the self-focusing arises from the optically induced modulation of the effective refractive index of a single photonics mode with an extraordinary polarization, boosted by the medium’s chirality²⁹. We call the first class spin-orbit optical solitons (as they are associated with spin-orbit couplings) and the second class bouncing optical solitons, with the index ‘EM’ (electromagnetic solitons) referring to either class.

When a toron and an optical soliton coexist, the total optical axis field can be obtained by summing the deviations $\delta\mathbf{n}^{\text{TS}}$ and $\delta\mathbf{n}^{\text{EM}}$ and the far-field \mathbf{n}_0 . Since the toron contains all optical axis field orientations, the general order of magnitude of the optical axis deviations for the topological soliton is approximately unity. To reveal the physical mechanisms behind our system, we focus here on the experimental and theoretical settings for which the magnitude of optical axis deviations for the optical soliton are weak (typically below 0.04).

Optical solitons exert a mechanical action on torons, as visible by the dynamical trajectories they adopt in our experiments (Fig. 1c). We model this optomechanical interaction by integrating the densities of force over the confined LC volume and writing a two-dimensional overdamped Langevin equation for the in-sample-plane trajectory \mathbf{R} of a toron (see Supplementary Section 3A):

$$\gamma \frac{d\mathbf{R}}{dt} = \mathbf{F}^{\text{L}} + \mathbf{F}^{\text{NL}} + \sqrt{2\gamma kT} \boldsymbol{\xi}. \quad (1)$$

Here, γ is the dissipation coefficient associated with viscous damping, kT is the thermal energy, $\boldsymbol{\xi}$ is a vector of zero-mean delta-correlated stationary Gaussian processes representing thermal fluctuations, \mathbf{F}^{L} (\mathbf{F}^{NL}) is the local (nonlocal) contribution to the total optical force \mathbf{F} , and t is time. Including thermal fluctuations enables measurement of the dissipation coefficient (see Supplementary Section 1B), thus unlocking the possibility of measuring optical forces from the experimentally observed velocity of the toron.

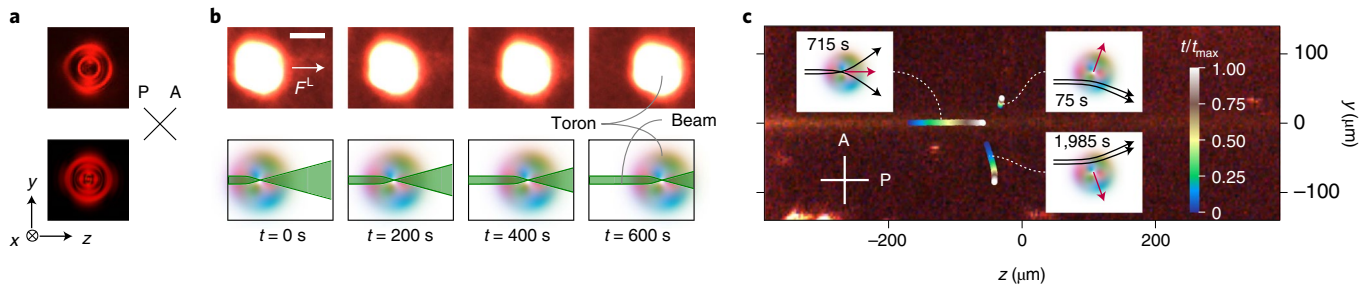


Fig. 3 | Spin-orbit soliton interactions with torons. **a**, Experimental (top) and simulated (bottom) unsaturated POM images of a toron. **b**, Saturated POM snapshots of a toron (top) pushed along a spin-orbit soliton propagating left to right and an associated physical interpretation in terms of the momentum deflection (bottom). Scale bar, 100 μm . **c**, An optical soliton micrograph like in Fig. 2e, overlaid with three trajectories of torons with different starting points relative to the beam. The continuous colour changes indicate the rescaled elapsed time for each trajectory, and the insets show the total trajectory elapsed times and the physical interpretation in terms of the momentum deflection.

The force \mathbf{F}^L is directly proportional to the opposite of the averaged deflection of light's momentum $\Delta\mathbf{p}$ (see Fig. 1d) and is therefore analogous to the optical force of laser tweezers. However, we emphasize that in our system the deflection of light's momentum is not due to discontinuities of material composition or density (for example, a laser acting on a particle) but instead is solely due to continuous changes of the optical axis. As such, the general properties of light's deflection in our system, and of the force field \mathbf{F}^L , are fully governed by the topology of torons. The dynamics of torons are further enriched by the force \mathbf{F}^{NL} , which is related to the interaction between the optical axis patterns \mathbf{n}^{TS} and \mathbf{n}^{EM} mediated by the orientational elasticity of the LC (see Fig. 1e). It has a highly nonlocal nature because the optically induced pattern \mathbf{n}^{EM} extends farther than the optical fields if the laser-beam waist is smaller than the thickness h of the sample—a condition that is satisfied in our experiments. It is calculated as minus the gradient of the elastic interaction energy (see Methods and Supplementary Section 3C), which is nonzero when the two patterns of optical axis overlap as in the bottom of Fig. 1e. The interplay between the force fields \mathbf{F}^L and \mathbf{F}^{NL} leads to extended control over the toron's dynamics illustrated for both optical solitons, with one of them showing tractor-beam-like features and multiple toron localization points (the pink 'along targets' of Fig. 1c) periodically decorating the optical soliton along its propagation. Below we use interchangeably \mathbf{n}^α or $\delta\mathbf{n}^\alpha \equiv \mathbf{n}^\alpha - \mathbf{n}_0$ (with $\alpha = \text{TS}$ or EM) to characterize the optical axis fields of topological and optical solitons.

Interaction between spin-orbit solitons and torons. We consider a spin-orbit soliton that propagates along the z axis (see Fig. 1c) in a 60- μm -thick sample. In Fig. 2a,b, we show experimental micrographs of light scattered out of the plane of the sample from the optical soliton, with an input beam power of $\sim 35\text{ mW}$ and $\leq 1\text{ mW}$, respectively. Since optical losses due to light scattering³⁷ slightly complicate the analysis of Fig. 2a,b, we evaluate self-focusing effects by plotting in Fig. 2c the rescaled intensity of the transverse profiles along the dashed lines L_{0-3} as a function of y/σ_p , with σ_p the input full-width at half-maximum (FWHM). This plot clearly shows that the visible spread of the transverse profile L_0 (the diffracting beam at weak power in Fig. 2c) can be compensated by nonlinear optical effects (profiles L_{1-3} associated with the self-focused beam of Fig. 2a). This observation is confirmed by examining Fig. 2d, which plots the FWHM as a function of the propagation distance z for the self-focused and diffracting beams of Fig. 2a,b.

The origin of the self-focusing lies in the optically induced reorientation in the optical axis field of the sample. Figure 2e presents a polarized optical micrograph (POM) of the sample with the laser filtered out. Therein, a bright colour corresponds to a nonzero

$[\delta\mathbf{n}^{EM}]$ associated with a beam-induced reorientation of the optical axis. Our simulations predict a periodic reorientation of the optical axis (Fig. 2f) due to the fast beatings between the orthogonal extraordinary and ordinary optical modes, mediated by nonlinear spin-orbit interactions. A cylindrical-glyph-based representation of the optical axis field is also shown with exaggerated reorientation angles and a stretched-out z direction in the bottom half of Fig. 2e. The periodicity of this optical axis pattern is not visible in the POM because the periodicity length $\Lambda \approx 2.2\ \mu\text{m}$ is smaller than the resolution of our microscope. The molecular reorientation mainly happens in the xy plane, with a 35 times weaker reorientation along z due to chirality. This resembles the pure xy reorientation of achiral media^{25–27,38,39}, as expected since here the cholesteric pitch is much bigger than the beam waist.

We numerically calculated the optical force fields that a spin-orbit soliton exerts on a toron, and estimated that \mathbf{F}^{NL} was always at least a thousand times weaker than \mathbf{F}^L , which means we can model the optomechanical interactions solely from the redistribution of light's momentum. This finding is expected since the periodicity length Λ associated with $\delta\mathbf{n}^{EM}$ is much smaller than the typical diameter of a toron in our sample (comparable to the sample thickness 60 μm). Indeed, the optical axis pattern \mathbf{n}^{EM} averaged over the diameter of the toron is almost identical to the far-field optical axis \mathbf{n}_0 and should therefore not lead to a substantial mechanical action when overlapping with the optical axis pattern \mathbf{n}^{TS} .

In Fig. 3b, we present a series of POM snapshots of a toron at different elapsed times. For convenient tracking, the microscope settings were adjusted to fully saturate the POM contrast inside the toron (see Fig. 3a for unsaturated images). The toron is pushed along a spin-orbit soliton perfectly aligned with its centre, due to the associated lensing effect⁴⁰ which transfers momentum from the light beam to the toron, as schematically shown in the bottom half of Fig. 3b. Alternatively, when the optical soliton is incident on the outer edge of the toron, the optical force \mathbf{F}^L pushes the toron sideways, away from the beam, as seen in Fig. 3c, which shows three experimental toron trajectories with different starting points on top of the POM image associated with the spin-orbit soliton. Each trajectory was captured independently in the same sample by optically creating, using a short laser pulse (see Supplementary Section 1A), the toron near a given starting point and destroying or moving away the toron at the end of the acquisition. We therefore emphasize that only a single toron was present at a given time inside the acquisition window. The insets of this figure show how the momentum of light is deflected for each particular starting point (black arrows), which allows the theoretical prediction of the general directions of the optical force (red arrows) in very good qualitative agreement with the experiment. In Supplementary Fig. 4, we present a direct

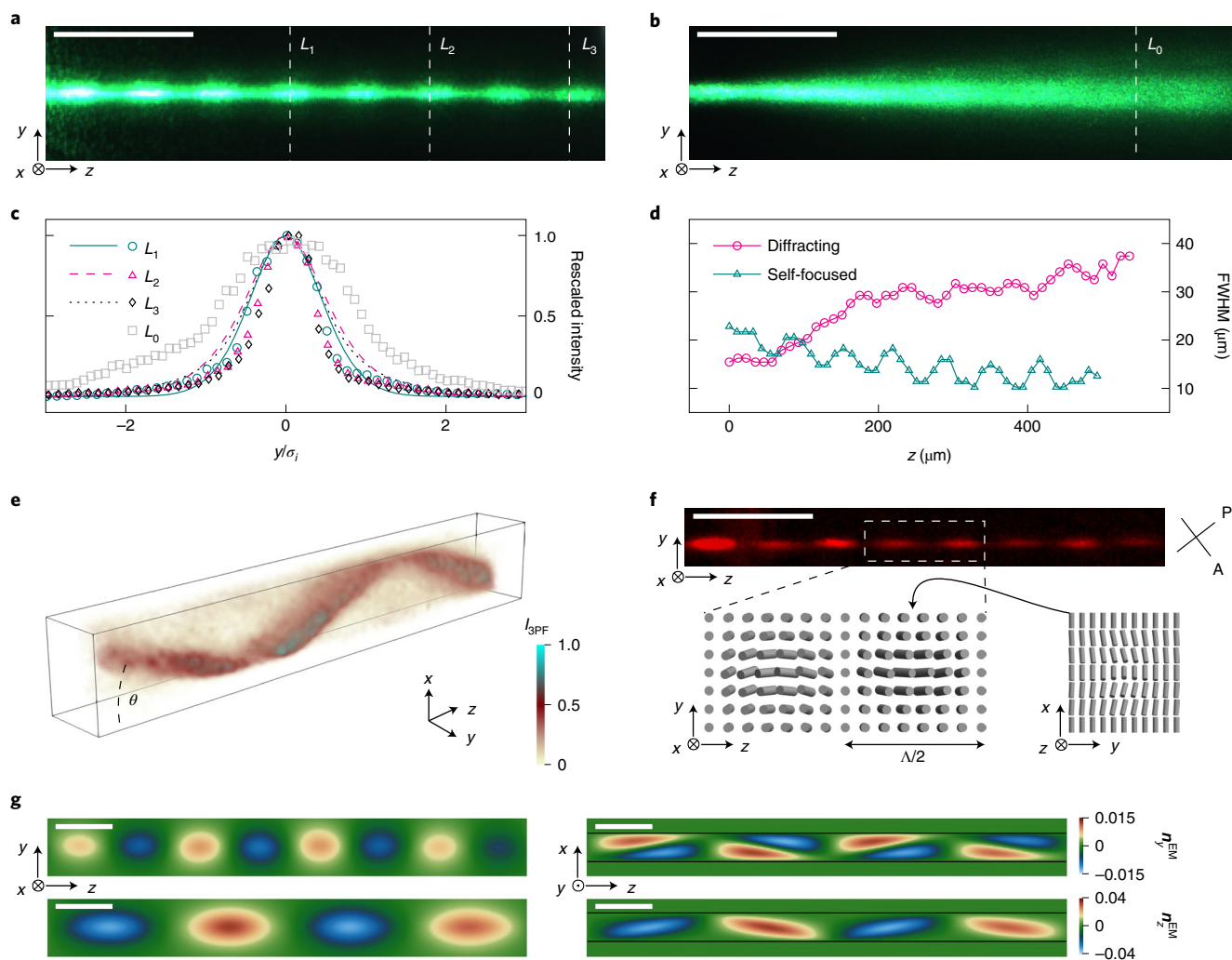


Fig. 4 | Properties of bouncing solitons. **a,b**, Optical micrographs of light scattered from a bouncing soliton propagating in a 17- μm -thick sample with a beam power of 35 mW (**a**) and $<1\text{ mW}$ (**b**). Scale bars represent the periodicity length $\Lambda = 128\ \mu\text{m}$. **c**, The transverse rescaled intensity profiles along the lines L_{0-3} in **a,b** as a function of y/σ_i , with σ_i the input FWHM. Symbols (lines) correspond to experimental (simulated) data. **d**, The FWHM values of the beams in **a,b** as a function of z . **e**, Volumetric rendering of the experimental tomography signal I_{3PF} showing the bouncing pattern of the optical soliton, where θ is the angle between the sample plane and the local axis of propagation. **f**, A POM image of the bouncing soliton in **a** (top) and schematic representation of the associated simulated optical axis field of periodicity Λ in the yz and xy planes (bottom) with exaggerated reorientation angles and a stretched-out z direction. Scale bar represents the periodicity length $\Lambda = 128\ \mu\text{m}$. **g**, Cross-sections of the simulated optical axis pattern associated with a bouncing soliton in a 10- μm -thick sample. Since the optical axis field has a unit-norm and is only weakly deformed, we show only its y and z components. Scale bars represent the periodicity length $\Lambda = 20\ \mu\text{m}$.

quantitative comparison between the experimental and simulated force profiles. The typical order of magnitude of the force rescaled by the beam power is $1\ \text{pN mW}^{-1}$ in experiments and simulations and depends on the sample thickness, birefringence and beam waist. We also note that the force field includes no equilibrium points because we focused on a simple regime where the toron's size is much bigger than the beating length Λ , which is a situation with no elastic interactions and is therefore analogous to a colloidal particle being pushed around by an unfocused laser. In the next section, we show that more complex behaviour arises when the toron's size is smaller than the typical lengths associated with bouncing solitons.

Interaction between bouncing solitons and torons. In Fig. 4, we summarize our main observations concerning the properties of bouncing optical solitons in a 17- μm -thick sample. Similar to spin-orbit solitons, the optically induced reorientation of the optical axis (bright red signal in Fig. 4f) enables the self-focusing of the laser

beam (Fig. 4a–d). However, a few important differences exist. First, and as already noted above and in Fig. 1c, the laser beam is not propagating along the z direction but is bouncing between the confining plates of the sample. In our simulations and experiments, the angle θ between the beam wavevector and the plane of the sample can either be imposed at the coupling interface or induced by scattering defects at the entrance. This angle is experimentally measured using a tomography experiment (see Methods and Fig. 4e), and here $\theta \approx 15^\circ$. Second, although the optically induced reorientation of the optical axis associated with both spin-orbit and bouncing solitons is periodic, the periodicity length Λ of the latter is much bigger than that of the former and can be estimated as $\Lambda \equiv 2h/\tan\theta \approx 128\ \mu\text{m}$ (Fig. 4f,g). Last, the chirality of the host medium has a much deeper influence on bouncing solitons than on the spin-orbit solitons of the previous section, since it induces a fully three-dimensional reorientation of the optical axis (Fig. 4g) and, overall, boosts the reorientation angle of the optical axis for a given beam power²⁹.

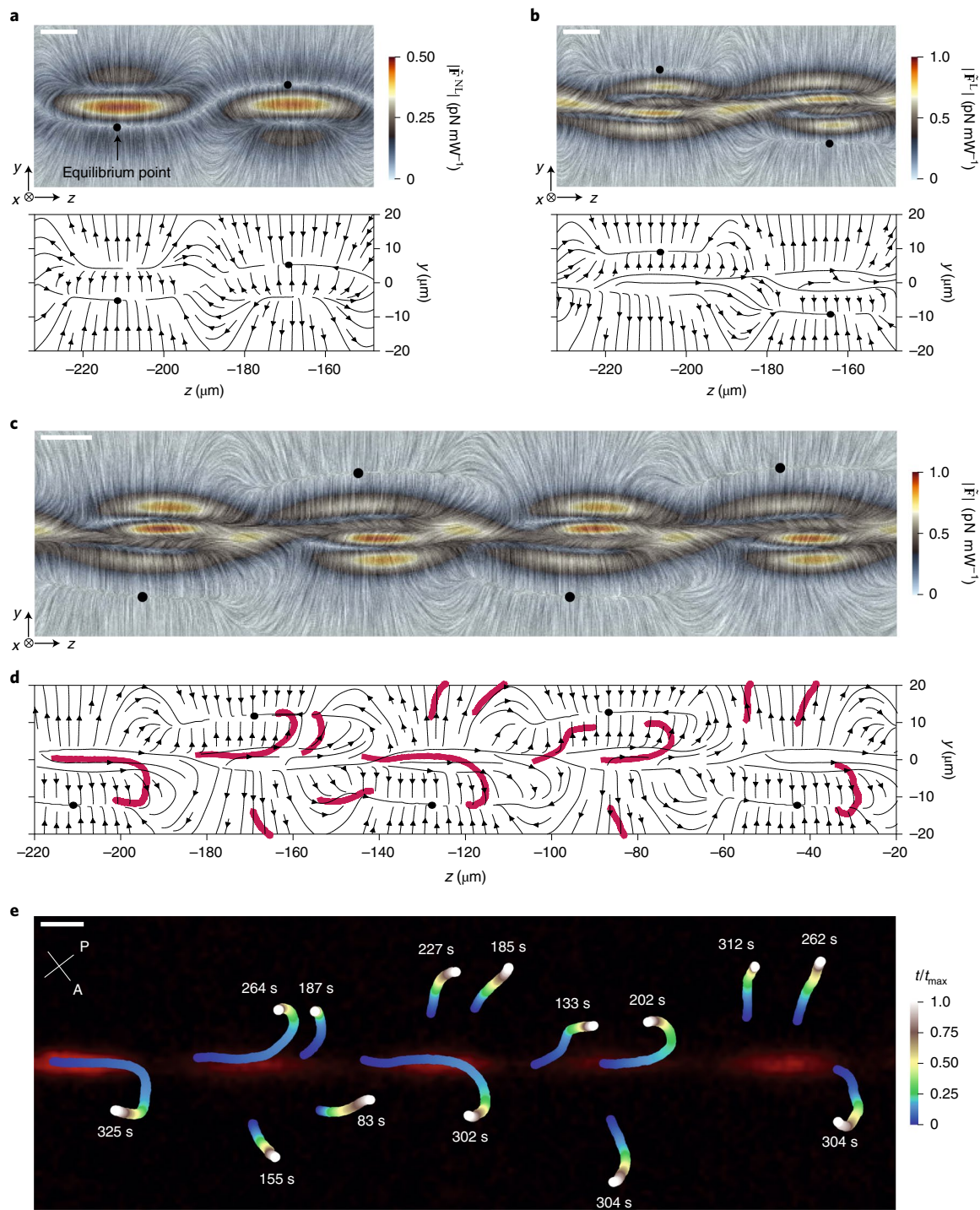


Fig. 5 | Bouncing optical soliton interactions with torons. **a**, Line-integral-convolution plot of the calculated force field \mathbf{F}^{NL} on top of a colour-coded image of $|\mathbf{F}^{NL}|$ (top), and associated force field lines in the same region of interest (bottom). **b**, Line-integral-convolution plot of the calculated force field \mathbf{F}^L on top of a colour-coded image of $|\mathbf{F}^L|$ (top), and associated force field lines in the same region of interest (bottom). **c**, Line-integral-convolution plot of the calculated total optical force field \mathbf{F} on top of a colour-coded image of $|\mathbf{F}|$. **d**, Direct comparison between experimentally observed toron trajectories (in red) and the force field lines of the calculated total optical force \mathbf{F} . **e**, Direct comparison between experimentally observed toron trajectories and force field lines of the calculated total optical force \mathbf{F} using the experimental POM image of the bouncing soliton in Fig. 4f as the background. Similar to Fig. 2, the continuous colour changes indicate the rescaled time for each trajectory and the white labels correspond to the total time associated with each trajectory. The sample thickness was $17\ \mu\text{m}$ in experiments and $10\ \mu\text{m}$ in simulations due to computational limitations, but a comparison can still be made due to the approximate scale invariance of the force field. Scale bars, $10\ \mu\text{m}$. Black dots in **a–d** represent the equilibrium points of the force fields.

Since the periodicity length $\Lambda \approx 128\ \mu\text{m}$ is now wider than the diameter of the torons ($\sim 30\text{--}40\ \mu\text{m}$), we can expect a non-negligible contribution of the force field \mathbf{F}^{NL} to the total optical force when the

optical axis patterns of the bouncing soliton and the torons overlap. Figure 5a,b confirms this expectation, by presenting the general shape of the numerically calculated optical force fields \mathbf{F}^{NL} and \mathbf{F}^L .

(see Supplementary Section 3) as well as their rescaled intensities $\tilde{F}^\alpha \equiv F^\alpha/P$ (with P the beam power and $\alpha \in \{L, NL\}$). The typical order of magnitude of both $|\tilde{F}^L|$ and $|\tilde{F}^{NL}|$ is 1 pNmW^{-1} , but both force fields are associated with complex spatial variations and multiple equilibrium points positioned periodically on each side of the beam. By summing F^L and F^{NL} , one obtains the total force F exerted on the toron plotted in Fig. 5c. The periodicity of this force field is directly related to the periodic pattern defining the bouncing soliton, and can be tuned by adjusting either the beam insertion angle θ or the sample thickness h . Furthermore, one can easily show, assuming perfect self-focusing and a fixed value for θ , that this force field is scale-invariant if all lengths (sample thickness, toron diameter and beam waist) are scaled by the same factor and the light's wavelength is much smaller than other lengths.

Using this scale invariance, Fig. 5d shows a direct comparison between the experimental realization of toron trajectories and the numerically calculated optical force field F . Similar to the previous section, each trajectory was measured independently with a single toron during a given duration inside the observation window. The trajectories follow the general field lines of the force fields, with some deviations due to thermal noise. This comparison therefore validates the overdamped Langevin model that we introduced above. Most interestingly, experiments and modelling reveal a wide range of trajectory shapes, including characteristic hook-like trajectories when the toron is translated towards one of the equilibrium points of the force field. This means that the optical force can go against the natural flow of light (left to right in all figures)—a phenomenon reminiscent of so-called tractor beams⁴¹, albeit here resulting in periodic arrays of spatially localized topological solitons on both sides of the optical soliton. This phenomenon can be interpreted in terms of nontrivial three-dimensional deflections of optical momentum and opto-elastic interactions arising from the complex optical patterns associated with the optical and topological solitons. In Supplementary Section 3, we describe the mechanisms yielding the force field of Fig. 5d and the drastic changes that can be induced by varying the material constants of the LC.

Discussion and conclusions

Our findings show how solitons embedded in different fields—molecular orientation and electromagnetic—can exhibit complex optomechanical interactions. We focused on the regime where the dynamics of topological solitons are largely predetermined by the direction of propagation and the type of optical soliton. However, this regime is just one of many possibilities. As another illustrative example, Supplementary Section 4 describes an interaction of optical solitons with surface-pinned torons and cholesteric fingers. The optical solitons in this case can be redirected by the topological solitons, as well as channelled out of the LC samples. Additional new possibilities can emerge from controlling the elasticity-mediated inter-soliton interactions between torons themselves⁴². Although we have so far explored the most basic situation of torons embedded in a uniform far-field background and interacting with each other repulsively through elasticity-mediated forces, such interactions can be controlled by applying electric fields, and even out-of-equilibrium dynamics can emerge⁴² when the amplitude of the applied voltage is modulated. Combining optical-topological inter-soliton interactions with these additional means of control could create a new paradigm of multi-stimuli-reconfigurable solitonic matter, although this falls outside the scope of this work.

A large range of physical behaviours can be anticipated between the two extremes at which the behaviour is dominated by either optical or topological solitons. For example, crystalline lattices of torons can have combinations of surface-pinned and mobile torons, with the latter objects acting as passive particle-like objects undergoing Brownian motion when no external forces are applied. Such topological solitons can typically be 'activated' by applying periodically

oscillating fields and patterns of light, both when moving individually and as periodic crystal-like arrays^{42–44}. These dynamics could then be enriched and guided by the interactions with optical solitons studied here. On the other hand, our quasi-two-dimensional study of interacting optical and topological solitons could be extended to higher dimensions, such as with spatio-temporal solitons called 'light bullets'⁴⁵ and with topological solitons like 'heliknotons' that are capable of forming three-dimensional crystalline arrays⁴⁶.

We anticipate that the experimental developments described above could go hand-in-hand with the introduction of a general topological optomechanical framework, enabling the determination of the mechanical interactions of chiral topological structures with general shaped beams of light. The theoretical model that we have introduced here is the first step towards this general framework, but the ultimate goal would be to account for all degrees of freedom of the structure being transported, which would enable the study of topological interactions between very generic patterns of optical and material fields. These multifield interactions could therefore nourish a very general line of research exploring the consequence of topology on multiple coupled fields of various natures (see, for example, the microfluidic system of ref. 47 or the charged topological colloids of ref. 48).

We foresee several applications based on the optomechanical interactions described here. For example, multiple optical solitons generating periodic equilibrium positions could be used to assist the self-assembly of colloidal metamaterials⁴⁹. Furthermore, the soliton-assisted manipulation of torons could find use in reconfiguring, in real-time, the various applications based on topological solitons^{40,50}, such as all-optical logical gates, circuits and memory. We emphasize that most of these photonics applications rely primarily on static configurations of LC order providing a given optical function (diffraction phase grating, beam deflector and so on), with dynamical rearrangement of the LC structures only needed for the device setup and/or reconfiguration. However, should the need arise, the dynamics of our system could be optimized with micrometre-thick samples (associated with a smaller dissipation coefficient γ), higher beam powers and an optical-soliton-induced director deformation of around unity, thus decreasing the typical timescales by up to a factor of 100.

Online content

Any methods, additional references, Nature Research reporting summaries, source data, extended data, supplementary information, acknowledgements, peer review information; details of author contributions and competing interests; and statements of data and code availability are available at <https://doi.org/10.1038/s41566-022-01002-1>.

Received: 18 July 2021; Accepted: 11 April 2022;

Published online: 30 May 2022

References

- Guo, B., Pang, X.-F., Wang, Y.-F. & Liu, N. *Solitons* (De Gruyter, 2018).
- Korteweg, D. J. & De Vries, G. On the change of form of long waves advancing in a rectangular canal, and on a new type of long stationary waves. *Lond. Edinb. Dubl. Philos. Mag. J. Sci.* **39**, 422–443 (1895).
- Philbin, T. G. et al. Fiber-optical analog of the event horizon. *Science* **319**, 1367–1370 (2008).
- Lautrup, B., Appali, R., Jackson, A. & Heimburg, T. The stability of solitons in biomembranes and nerves. *Eur. Phys. J. E* **34**, 57 (2011).
- Skyrme, T. H. R. Particle states of a quantized meson field. *Proc. R. Soc. Lond. A* **262**, 237–245 (1961).
- Frieman, J. A., Olinto, A. V., Gleiser, M. & Alcock, C. Cosmic evolution of nontopological solitons. *Phys. Rev. D* **40**, 3241–3251 (1989).
- Shnir, Y. M. Gravitating Hopfions. *J. Exp. Theor. Phys.* **121**, 991–997 (2015).
- Shnir, Y. M. *Topological and Non-Topological Solitons in Scalar Field Theories* (Cambridge Univ. Press, 2018).
- Chen, Z., Segev, M. & Christodoulides, D. N. Optical spatial solitons: historical overview and recent advances. *Rep. Prog. Phys.* **75**, 086401 (2012).

10. Stegeman, G. I. & Segev, M. Optical spatial solitons and their interactions: universality and diversity. *Science* **286**, 1518–1523 (1999).
11. Conti, C., Peccianti, M. & Assanto, G. Observation of optical spatial solitons in a highly nonlocal medium. *Phys. Rev. Lett.* **92**, 113902 (2004).
12. Assanto, G. (ed.) *Nematicons: Spatial Optical Solitons in Nematic Liquid Crystals* (Wiley, 2013).
13. Assanto, G. & Smyth, N. F. Self-confined light waves in nematic liquid crystals. *Physica D* **402**, 132182 (2020).
14. Peccianti, M., Conti, C., Assanto, G., De Luca, A. & Umetsu, C. Routing of anisotropic spatial solitons and modulational instability in liquid crystals. *Nature* **432**, 733–737 (2004).
15. Peccianti, M., Dyadyusha, A., Kaczmarek, M. & Assanto, G. Tunable refraction and reflection of self-confined light beams. *Nat. Phys.* **2**, 737–742 (2006).
16. Peccianti, M., Assanto, G., Dyadyusha, A. & Kaczmarek, M. Nonspecular total internal reflection of spatial solitons at the interface between highly birefringent media. *Phys. Rev. Lett.* **98**, 113902 (2007).
17. Piccardi, A., Assanto, G., Lucchetti, L. & Simoni, F. All-optical steering of soliton waveguides in dye-doped liquid crystals. *Appl. Phys. Lett.* **93**, 171104 (2008).
18. Izdebskaya, Y. V., Desyatnikov, A. S. & Kivshar, Y. S. Self-induced mode transformation in nonlocal nonlinear media. *Phys. Rev. Lett.* **111**, 123902 (2013).
19. Alberucci, A., Piccardi, A., Kravets, N., Buchnev, O. & Assanto, G. Soliton enhancement of spontaneous symmetry breaking. *Optica* **2**, 783–789 (2015).
20. Kravets, N. et al. Bistability with optical beams propagating in a reorientational medium. *Phys. Rev. Lett.* **113**, 023901 (2014).
21. Perumbilavil, S. et al. Beaming random lasers with soliton control. *Nat. Commun.* **9**, 3863 (2018).
22. Fratolocchi, A., Assanto, G., Brzdąkiewicz, K. A. & Karpierz, M. A. Discrete light propagation and self-trapping in liquid crystals. *Opt. Express* **13**, 1808–1815 (2005).
23. Henninot, J., Debailleul, M. & Warengem, M. Tunable non-locality of thermal non-linearity in dye doped nematic liquid crystal. *Mol. Cryst. Liq. Cryst.* **375**, 631–640 (2002).
24. Piccardi, A., Alberucci, A., Tabiryan, N. & Assanto, G. Dark nematicons. *Opt. Lett.* **36**, 1356–1358 (2011).
25. Karpierz, M. A. Solitary waves in liquid crystalline waveguides. *Phys. Rev. E* **66**, 036603 (2002).
26. Jisha, C. P., Alberucci, A., Beeckman, J. & Nolte, S. Self-trapping of light using the Pancharatnam–Berry phase. *Phys. Rev. X* **9**, 021051 (2019).
27. Assanto, G. & Smyth, N. F. Spin-optical solitons in liquid crystals. *Phys. Rev. A* **102**, 033501 (2020).
28. Laudyn, U. A., Kwasny, M. & Karpierz, M. A. Nematicons in chiral nematic liquid crystals. *Appl. Phys. Lett.* **94**, 091110 (2009).
29. Poy, G., Hess, A. J., Smalyukh, I. I. & Žumer, S. Chirality-enhanced periodic self-focusing of light in soft birefringent media. *Phys. Rev. Lett.* **125**, 077801 (2020).
30. Lam, L. & Prost, J. (eds) *Solitons in Liquid Crystals* (Springer, 2012).
31. Smalyukh, I. I. Review: knots and other new topological effects in liquid crystals and colloids. *Rep. Prog. Phys.* **83**, 106601 (2020).
32. Smalyukh, I. I., Lansac, Y., Clark, N. A. & Trivedi, R. P. Three-dimensional structure and multistable optical switching of triple-twisted particle-like excitations in anisotropic fluids. *Nat. Mater.* **9**, 139–145 (2010).
33. Ackerman, P. J. & Smalyukh, I. I. Diversity of knot solitons in liquid crystals manifested by linking of preimages in torons and hopfions. *Phys. Rev. X* **7**, 011006 (2017).
34. Oswald, P., Baudry, J. & Pirkel, S. Static and dynamic properties of cholesteric fingers in electric field. *Phys. Rep.* **337**, 67–96 (2000).
35. Ackerman, P. J. et al. Laser-directed hierarchical assembly of liquid crystal defects and control of optical phase singularities. *Sci. Rep.* **2**, 414 (2012).
36. Loussert, C. & Brasselet, E. Multiple chiral topological states in liquid crystals from unstructured light beams. *Appl. Phys. Lett.* **104**, 051911 (2014).
37. Hu, C. & Whinnery, J. R. Losses of a nematic liquid-crystal optical waveguide. *J. Opt. Soc. Am.* **64**, 1424–1432 (1974).
38. Karpierz, M. A., Sierakowski, M., Świlło, M. & Woliński, T. Self focusing in liquid crystalline waveguides. *Mole. Cryst. Liq. Cryst. A* **320**, 157–163 (1998).
39. Kwasny, M. et al. Self-guided beams in low-birefringence nematic liquid crystals. *Phys. Rev. A* **86**, 013824 (2012).
40. Hess, A. J., Poy, G., Tai, J.-S. B., Žumer, S. & Smalyukh, I. I. Control of light by topological solitons in soft chiral birefringent media. *Phys. Rev. X* **10**, 031042 (2020).
41. Chen, J., Ng, J., Lin, Z. & Chan, C. Optical pulling force. *Nat. Photonics* **5**, 531–534 (2011).
42. Sohn, H. R. & Smalyukh, I. I. Electrically powered motions of toron crystallites in chiral liquid crystals. *Proc. Natl. Acad. Sci. USA* **117**, 6437–6445 (2020).
43. Sohn, H. R., Liu, C. D. & Smalyukh, I. I. Schools of skyrmions with electrically tunable elastic interactions. *Nat. Commun.* **10**, 4744 (2019).
44. Sohn, H. R., Liu, C. D., Wang, Y. & Smalyukh, I. I. Light-controlled skyrmions and torons as reconfigurable particles. *Opt. Express* **27**, 29055–29068 (2019).
45. Minardi, S. et al. Three-dimensional light bullets in arrays of waveguides. *Phys. Rev. Lett.* **105**, 263901 (2010).
46. Tai, J.-S. B. & Smalyukh, I. I. Three-dimensional crystals of adaptive knots. *Science* **365**, 1449–1453 (2019).
47. Giomi, L., Kos, Ž., Ravnik, M. & Sengupta, A. Cross-talk between topological defects in different fields revealed by nematic microfluidics. *Proc. Natl. Acad. Sci. USA* **114**, E5771–E5777 (2017).
48. Everts, J. C. & Ravnik, M. Complex electric double layers in charged topological colloids. *Sci. Rep.* **8**, 14119 (2018).
49. Aplinc, J., Pusovnik, A. & Ravnik, M. Designed self-assembly of metamaterial split-ring colloidal particles in nematic liquid crystals. *Soft Matter* **15**, 5585–5595 (2019).
50. Fert, A., Reyren, N. & Cros, V. Magnetic skyrmions: advances in physics and potential applications. *Nat. Rev. Mater.* **2**, 17031 (2017).

Publisher's note Springer Nature remains neutral with regard to jurisdictional claims in published maps and institutional affiliations.

© The Author(s), under exclusive licence to Springer Nature Limited 2022

Methods

Preparation of LC samples with topological solitons. Each experimental cell consists of an LC layer sandwiched between two glass plates treated for perpendicular boundary conditions (homeotropic anchoring)^{31,32}. To define the thickness between the glass plates, we placed ultraviolet (UV) curable dot-like glue droplets (NOA-65, Norland Optical) near the corners of the cell volume, containing silica spacer spheres with a diameter of 16.9 μm or 60 μm (ThermoFisher). Before curing, we confirmed that the top and bottom plate edges along a single side were flush with each other to minimize LC director distortion near the point of entrance of the beam. For the 60- μm -thick cells, a treated coverslip was added on the optical-insertion interface so that the optical axis field of the LC stays uniform and normal to the sample plate. By the application of a weak UV illumination source, the UV glue was cured until hard in 30 min.

The cells were filled with a cholesteric LC via capillary force. In most experiments, the LC was a mixture of a nematic LC (E7, Shijiazhuang Chengzhi Yonghua Display Materials) with a chiral dopant (cholesteryl pelargonate, SigmaAldrich). The only exception was the three-photon-fluorescence (3PF) imaging experiment, where we prepared and used a mixture that photo-polymerized into an LC gel to preserve optically induced perturbations around an optical soliton^{29,33}. The main output of this experiment was the three-photon-absorption-based fluorescence signal $I_{3\text{PP}}$ whose deviation from zero corresponds to the core of the optical soliton due to partial photo-polymerization induced by the laser before full photo-polymerization via UV light. The signal $I_{3\text{PP}}$ therefore corresponds to a direct trace of the local intensity of the laser in our experiments, which enabled us to reconstruct the path of the beam in the sample and observe the associated bouncing pattern of Fig. 4e. Note that, in general, such bouncing patterns are not due to the chirality of the medium—similar patterns have been observed in achiral samples with various boundary conditions^{54–56}—but are due either to a boundary-induced modulation of the photonics potential (as in the previously cited paper) or to total internal reflection at the confining boundaries (as in this paper).

In all experiments, we adjusted the cholesteric pitch so that the cell had a thickness-to-pitch (d/p) ratio of approximately 0.8–1.0. These particular cell specifications enabled a uniform optical axis background to be obtained normal to the sample plates with selectively generated topological solitons. The torons were generated on demand at desired spatial locations within the LC cell with the point-wise application of scanned infrared continuous-wave laser tweezers to the LC sample^{32,33}. As described in refs. 35,40, an in-sample optical power of 30–160 mW was sufficient to temporarily reorient the cholesteric LC director and locally transition from the far-field LC orientation to an energetically favourable toron state. The experimental setup associated with our laser tweezers is described in more detail in Supplementary Section 1A.

Observations and analysis of inter-soliton interactions. The types of interaction behaviour were captured between spin-orbit and unpinned topological solitons as well as between bouncing optical solitons and both pinned and unpinned topological solitons. In the pinned case, the boundary conditions of the glass plates confining the chiral LC were perturbed using laser tweezers such that the topological solitons energetically favoured pinning to the substrate. A pinned topological soliton is therefore fixed in place and can only deflect light. Conversely, unpinned topological solitons are able to freely diffuse throughout the sample plane and can be transported along the field lines of the optical forces described in the main text. For this work, different types of LC sample cell were prepared for pinned and unpinned topological solitons, where both types of soliton could be optically generated at different laser powers and erased by applying electric fields. The main text focuses on the fascinating dynamical trajectories of unpinned torons, whereas the additional types of interaction behaviour of optical solitons with pinned topological solitons are described in Supplementary Section 4.

In-sample-plane optical coupling with monochromatic Gaussian beams and through-sample-plane visualization of the topological solitons and their optomechanical behaviour were carried out using a custom-built experimental setup described in Supplementary Fig. 1. This laser setup enabled us to adjust the incident beam's power, waist, linear polarization and tilt angle, and to couple it through the side of the sample as shown in Fig. 1c,d. In all experiments, the wavelength of the laser light was 532 nm and the power of the incident beam was varied between 1 and 80 mW. We emphasize that the temperature can be considered as constant since the thermal absorption is negligible in our system at these beam powers. Observations of the interactions between topological and optical solitons were carried out using an Olympus IX-73 optical microscope. Scattered light from the laser beam associated with the optical soliton was captured by shutting off the white-light source of the microscope and keeping only the microscope objective between the sample and the camera. These observations correspond to the green-coloured images of Figs. 2 and 4. Conversely, the optical axis field patterns associated with the topological and optical solitons were characterized by filtering out the light scattered from the laser using a red bandpass filter and capturing transmission-mode optical micrographs of the sample under crossed polarizers. These observations correspond to the red-coloured images of Figs. 2–5.

To automatically deduce the motion trajectory of a toron from an experimentally obtained temporal stack of microscope images, we implemented

a custom-tracking algorithm using Python. This algorithm works with three steps for each image of the stack: first, the original image is binarized with an appropriate threshold; then, the convex hull of this thresholded image is calculated; finally, the vertices of the convex hull are fitted with a circle, whose centre constitutes the output of the algorithm for a given stack index. All calculations were made using the NumPy and SciPy libraries^{57,58}. The advantage of this approach in comparison with state-of-the-art particle trackers for soft matter is that it is very robust with respect to the toron appearance in the microscope, which varies due to the polarized illumination and complex pattern of the optical axis. Although one can partially circumvent this problem by acquiring very saturated images, as in Fig. 3b, this approach is not ideal due to variations of intensity when the toron is moving. Using a convex hull enabled us to solve this problem and yielded a visually unbiased estimation of the centre, even when the observed toron was not a perfectly uniform and bright disc.

In Supplementary Section 1A, we give the experimental details and schematics of the utilized optical setups, especially concerning the laser generation of topological and optical solitons and their quantitative characterization using various optical techniques. Although the experimental results are presented for one wavelength, 532 nm, for consistency, there are no fundamental limitations on exploring and technologically utilizing such phenomena at other visible or near-infrared wavelengths, say at the telecommunication wavelength, as long as the medium is transparent at the corresponding wavelength of light.

Modelling of optical forces. Since the force \mathbf{F}^{L} has been defined as the local contribution to the optical force due to the deflection of light's momentum, it can be readily obtained by integrating the flux of Maxwell's stress tensor σ^{EM} through a surface S enclosing the toron⁵⁹:

$$\mathbf{F}^{\text{L}} \equiv \int_S \sigma^{\text{EM}} \cdot d\mathbf{S} \quad (2)$$

We calculated this force based on either an exact calculation of Maxwell's stress tensor or a simplified version of this tensor in the limit of geometrical optics.

In the first method, an accurate wide-angle beam-propagation simulation is performed to model the transformation of the laser beam near the toron, based on a novel numerical scheme⁶⁰. Then, the stress tensor field of Maxwell is directly calculated from the numerically simulated optical fields \mathbf{E} , \mathbf{D} , \mathbf{B} and \mathbf{H} , using its general expression⁶¹. Finally, the flux integral of σ^{EM} through the computational mesh is calculated to obtain the force \mathbf{F}^{L} for a given position of the toron with respect to the laser beam.

In the second method, the expression of Maxwell's stress tensor is first simplified in the geometrical optical limit. On the basis of the ray-tracing formalism and energy-conservation laws⁶², we then demonstrated (see Supplementary Section 3B) that

$$\mathbf{F}^{\text{L}} = - \int_{\Sigma} \frac{j(u, v) \Delta \mathbf{p}(u, v)}{c} du dv, \quad (3)$$

where c is the speed of light, Σ is an eikonal surface of the incident light rays parameterized by the transverse coordinates u and v , $\Delta \mathbf{p}$ is the deflection of the renormalized wavevector $\mathbf{p} = \mathbf{k}/k_0$ (with \mathbf{k} the wavevector and k_0 the wavevector in empty space) before and after crossing the toron, and $j \equiv q[\mathbf{S} \cdot \mathbf{p}]$ is the density of energy flux along eikonals (with q the geometrical spreading and \mathbf{S} the Poynting vector). We numerically calculate this integral directly from the ray-tracing method described in ref. 62. This second method is approximate, but fast and accurate; it was deployed for all the calculations, whereas the first method was used to validate it (see Supplementary Section 3B).

We remark that the momentum deflection $\Delta \mathbf{p}$ is primarily due to the modulation of the beam walkoff inside topological solitons. Using the beam-propagation approach, this modulation is directly taken into account with the so-called 'walkoff operator'⁶⁰, whose importance was first recognized (with different notations) by Assanto and collaborators¹². Using the ray-tracing approach, this modulation is directly embedded in the variation of the underlying Hamiltonian⁶². In both cases, only the extraordinary polarization of the beam is sensitive to this modulation, which is why bouncing solitons can preserve their solitonic nature after interaction (single extraordinary mode) whereas spin-orbit solitons cannot (mixed extraordinary and ordinary modes), as detailed in Supplementary Section 3B.

The force \mathbf{F}^{NL} is the nonlocal contribution to the optical force mediated by the orientational elasticity of the LC medium. Its calculation relies on the elastic interaction energy G of the liquid crystal volume Ω between the optical axis patterns \mathbf{n}^{TS} and \mathbf{n}^{EM} that are respectively associated with the toron and the optical soliton:

$$G = \int_{\Omega} \sum_{\alpha, \beta=y,z} n_{\alpha}^{\text{EM}} L_{\alpha\beta} n_{\beta}^{\text{TS}} dV, \quad (4)$$

where L is a self-adjoint matrix differential operator that characterizes the orientational elasticity of the medium (see Supplementary Section 3C). We note that G becomes nonzero once the localized patterns $\delta \mathbf{n}^{\text{TS}}$ and $\delta \mathbf{n}^{\text{EM}}$ overlap

(Fig. 1e). We numerically calculate this interaction energy using the simulated optical axis patterns \mathbf{n}^{TS} and \mathbf{n}^{EM} for different shifts \mathbf{R} of the toron with respect to the optical soliton, and then deduce the nonlocal optical force field as $\mathbf{F}^{\text{NL}} = -\nabla_{\mathbf{R}}G$. Simulations of the internal structure of topological and optical solitons were carried out using the numerical methods described elsewhere^{29,60} and detailed in Supplementary Section 2.

Data availability

All data and postprocessing scripts are available from the Zenodo repository (<https://doi.org/10.5281/zenodo.6394431>). Polarized optical microscopy simulations were performed using the open-source software Nemaktis (<https://github.com/warthan07/Nemaktis> and <https://doi.org/10.5281/zenodo.4695959>).

References

- Pandey, M. et al. Self-assembly of skyrmion-dressed chiral nematic colloids with tangential anchoring. *Phys. Rev. E* **89**, 060502 (2014).
- Pandey, M. et al. Topology and self-assembly of defect-colloidal superstructure in confined chiral nematic liquid crystals. *Phys. Rev. E* **91**, 012501 (2015).
- Evans, J. S., Ackerman, P. J., Broer, D. J., van de Lagemaat, J. & Smalyukh, I. I. Optical generation, templating, and polymerization of three-dimensional arrays of liquid-crystal defects decorated by plasmonic nanoparticles. *Phys. Rev. E* **87**, 032503 (2013).
- Peccianti, M., Fratolocchi, A. & Assanto, G. Transverse dynamics of nematicons. *Opt. Express* **12**, 6524–6529 (2004).
- Alberucci, A., Peccianti, M. & Assanto, G. Nonlinear bouncing of nonlocal spatial solitons at the boundaries. *Opt. Lett.* **32**, 2795–2797 (2007).
- Alberucci, A. et al. Modulation analysis of boundary-induced motion of optical solitary waves in a nematic liquid crystal. *Phys. Rev. A* **79**, 043816 (2009).
- Harris, C. R. et al. Array programming with NumPy. *Nature* **585**, 357–362 (2020).
- Virtanen, P. et al. SciPy 1.0: fundamental algorithms for scientific computing in Python. *Nat. Methods* **17**, 261–272 (2020).
- Nieminen, T. A. et al. Optical tweezers: theory and modelling. *J. Quant. Spectrosc. Radiat. Transf.* **146**, 59–80 (2014).
- Poy, G. & Žumer, S. Physics-based multistep beam propagation in inhomogeneous birefringent media. *Opt. Express* **28**, 24327–24342 (2020).
- Piccirillo, B. & Santamato, E. Light angular momentum flux and forces in birefringent inhomogeneous media. *Phys. Rev. E* **69**, 056613 (2004).
- Poy, G. & Žumer, S. Ray-based optical visualisation of complex birefringent structures including energy transport. *Soft Matter* **15**, 3659–3670 (2019).

Acknowledgements

Experimental research at CU-Boulder was supported by the National Science Foundation through grant DMR-1810513 (A.J.H., A.J.S., M.P. and I.I.S.). G.P. and S.Ž. acknowledge funding from the ARSS (Javna Agencija za Raziskovalno Dejavnost RS) through grant P1-0099 and from the European Union's Horizon 2020 programme through the Marie Skłodowska-Curie grant agreement no. 834256 and COST European Topology Interdisciplinary Action (EUTOPIA CA17139). A.J.H. thanks the United States' Office of Science Graduate Student Research (SCGSR) Fellowship for partial project support. A.J.H. also thanks the United States' National Renewable Energy Laboratory and its Technology Transfer Office for remuneration from the Technology Licensing and Commercialization Fellowship while data were analysed and the manuscript was written. I.I.S. also acknowledges the hospitality of the Chirality Research Center (CResCent) at the University of Hiroshima, Japan, during his sabbatical stay, where he was partly working on this article. We thank P. Ackerman, Y. Yuan, T. Lee and H. Mundoor for discussions.

Author contributions

A.J.H., A.J.S. and M.P. performed the experiments. A.J.H. built the experimental setup and oversaw the systematic collection of experimental data. A.J.H. and G.P. analysed the data. G.P. wrote postprocessing scripts to analyse experimental toron trajectories, designed the theoretical framework and realized numerical simulations to explain the experimental findings. G.P., A.J.H., S.Ž. and I.I.S. wrote the paper, with feedback from all authors. I.I.S. conceived the project and initiated the collaboration. S.Ž. supervised the theoretical research and I.I.S. supervised the experimental research.

Competing interests

The authors declare no competing interests.

Additional information

Supplementary information The online version contains supplementary material available at <https://doi.org/10.1038/s41566-022-01002-1>.

Correspondence and requests for materials should be addressed to Ivan I. Smalyukh.

Peer review information *Nature Photonics* thanks Alexander Szameit and the other, anonymous, reviewer(s) for their contribution to the peer review of this work.

Reprints and permissions information is available at www.nature.com/reprints.